ROYAL SOCIETY
OF CHEMISTRY

PAPER

Check for updates

Robust graphene-drum bridged carbon aerogels for broadband acoustic and electromagnetic attenuation†

Yijing Zhao,[a] Tianxiao Niu,[a] Xinyu Dong,[a] Yong Yang*[b] and Wei Zhai ![ORCID] *[a]

The rapid growth of wireless technologies and urban development has led to a concerning increase in acoustic and electromagnetic pollution. Herein, we have developed robust graphene-drum bridged carbon aerogels (Gd-CAs) as a solution for broadband dual-wave attenuation. The Gd-CAs demonstrate exceptional properties including light weight, high robustness (150 kPa at 80% compression strain), and excellent compression fatigue resistance (1000 cycles at 50% strain). The interconnected graphene-drums within the carbon truss structures facilitate synergistic dissipation of acoustic energy, leading to excellent acoustic absorption across a broad frequency range with a noise reduction coefficient of 0.59. The binary 3D conductive drum and strut pathways in Gd-CAs provide an enhanced dielectric loss pathway, resulting in an effective attenuation bandwidth of 8.2 GHz, making Gd-CAs superior candidates for broadband electromagnetic wave attenuators. Moreover, Gd-CAs have multiple functions such as waterproofing, nonflammability, thermal insulation, and strain-sensing, thereby enhancing their suitability for diverse practical applications. The proposed graphene-drum bridged carbon aerogels provide a compelling strategy to address the pressing need to mitigate electromagnetic and acoustic pollution in various applications.

1. Introduction

In the face of exponential advancements in wireless communication, aerospace technologies, electronic equipment, and urban infrastructure, we confront an escalating issue: the increasing severity of acoustic and electromagnetic wave pollution. These ubiquitous but invisible pollutants not only pose risks to human health but also disrupt the normal operation of wireless devices.[1,2] Addressing this growing concern calls for the development of dual-wave pollution attenuators. However, designing attenuators for acoustic and electromagnetic waves requires distinct approaches due to their inherent differences.[3] Acoustic waves are influenced by the porous structures of acoustic absorbers, while electromagnetic waves undergo attenuation based on the dielectric or magnetic properties of the propagation medium.[4,5] Promisingly, graphene-based porous materials demonstrate potential for acoustic and electromagnetic energy attenuation due to their porous microstructure and intrinsically excellent conductivity.[6,7]

The tunable porosity and resonant effect of thin graphene sheets in graphene-based porous materials contribute to their capability for efficient sound absorption.[8,9] Recent studies have proposed and demonstrated effective sound absorption performance in graphene-based foams[10,11] and polymer–graphene porous composites.[12–15] However, graphene foams often face reliability and structural integrity issues due to weak van der Waals forces bonding the graphene sheets, while polymer–graphene composites can lead to collapse and aggregation of the graphene sheets, which severely impact their acoustic absorption efficacy.[7,9–11] Therefore, the development of structurally controllable graphene-porous materials with mechanical durability for broadband acoustic absorption is crucial.

Graphene-based porous materials exhibit potential as electromagnetic wave (EMW) attenuators, with the graphene sheets serving as dielectric loss components, while their porous structures enable multiple internal reflections and scattering.[16] This unique combination enhances their ability to capture and attenuate EMW energy effectively. However, the low dielectric-dominated loss mechanism restricts the EMW attenuation efficiency of graphene porous materials to a narrow frequency bandwidth. Efforts to enhance their attenuation capabilities involve the incorporation of magnetic[17,18] or conductive second phases[19] to enhance the loss capabilities. Nonetheless, the second phase introduction often compromises structural stability or brings about defects that weaken mechanical properties.[16] Therefore, the development of graphene-based porous

[a]Department of Mechanical Engineering, National University of Singapore, 117575, Singapore. E-mail: mpezwei@nus.edu.sg

[b]National University of Singapore, 5A Engineering Drive 1, 117411, Singapore. E-mail: tslyayo@nus.edu.sg

† Electronic supplementary information (ESI) available. See DOI: https://doi.org/10.1039/d3ta04895k

This journal is © The Royal Society of Chemistry 2023

materials with controllable structural integrity, tunable dielectric properties, and mechanical reliability is of significant significance to overcome these challenges and achieve broadband attenuation of both acoustic and EMW pollution.

In this study, we present the development of robust and multifunctional graphene-drum bridged carbon aerogels (Gd-CAs) for broadband dual attenuation of acoustic and electromagnetic pollution. These Gd-CAs are fabricated *via* an infiltration–freeze–drying process, in which self-aligned graphene sheets bridge over the cellular faces of carbon aerogels, forming stable edge-to-edge drum-like connections. We have done microstructure analysis and mechanical testing to understand their relationship, and the optimal Gd-CA exhibits high robustness (withstanding up to 150 kPa at 80% compression strain) and fatigue durability (1000 cycles at 50% strain). The Gd-CA shows effective broadband sound absorption with a noise reduction coefficient (NRC) of 0.59 due to a synergistic dissipation of resonance induced by thin graphene-drums and the enhanced viscous loss by the semi-open porous cavity. Moreover, the Gd-CA has an effective attenuation bandwidth (EAB) of 8.2 GHz as a promising broadband EMW attenuator. Numerical analysis has confirmed that the enhanced EMW attenuation is caused by an enhanced impedance matching and increased internal reflections, conduction loss, and polarization relaxation losses due to the binary 3D conductive channels. Additionally, the Gd-CAs demonstrate waterproofing, nonflammability, thermal insulation, and strain sensing capabilities, endowing them with potential for practical applications. This significant advancement addresses the urgent need for dual attenuation of acoustic and electromagnetic pollution, and the promising features of Gd-CAs in terms of robustness, multifunctionality, and mechanical durability make them promising for various fields, including aviation, engineering, and civil applications.

2. Results and discussion

2.1 Fabrication and structural characterization

The fabrication process of graphene-drum bridged carbon aerogels (Gd-CAs) is illustrated in Fig. 1a and Section S1, ESI.† Firstly, commercially available melamine foams (MFs) (Fig. S1a†) undergo carbonization to form carbon aerogels (CAs), which possess a 3D interconnected open-cell porous structure, as shown in the SEM image in Fig. 1b and S1b.† Subsequently, the CAs are entirely immersed in graphene oxide (GO) suspensions through vacuum infiltration and subjected to freezing. During this freezing stage, ice crystals start forming within the cavities of the CAs' cellular structures. The advancing ice front compels the suspended GO sheets, eventually compressing them between the cellular faces and establishing interconnected GO thin film interfaces.[12,20] After the ice crystals are eliminated *via* freeze-drying, the GO thin films remain supported by the trusses of the CAs' cellular structures, forming drum-like faces that interconnect the strut skeletons. This infiltration–freezing–drying cycle can be repeated to increase the number of GO-drums. The final stage is a thermal reduction process that transforms the GO-drums into graphene-drums,

yielding the final products of graphene-drum bridged carbon aerogels (Gd-CAs), as shown in the SEM images in Fig. 1c–e. The samples Gd-CA-1, Gd-CA-2, and Gd-CA-3 were prepared with 1, 2, and 3 repetitions of the infiltration–freezing–drying processes, respectively. Notably, with an increase in the number of repetitions, the formation of graphene-drums leads to the expansion of interconnected faces within the CA cells, as shown in Fig. 1c–e. Detailed views of the graphene drums stretched over the CA trusses and interconnected at the edges are provided in Fig. 1h and S2.† The images show the graphene-drums layered across the CA trusses, with their thickness increasing as the infiltration process is repeated, especially noticeable in the sample Gd-CA-3 (Fig. S2b†). Fig. 1i provides cross-section SEM images that further depict the thin-film morphology of the graphene-drums in the sample Gd-CA-2, exhibiting thicknesses less than 1 μm and resembling bulging drums spanning the trusses. In addition, the highly porous microstructure of Gd-CAs provides them with ultralightweight properties, allowing them to maintain low density with extensive graphene-drum incorporation. The densities of the samples are 9.8 mg cm^{-3}, 13.9 mg cm^{-3}, 21.8 mg cm^{-3}, and 35.6 mg cm^{-3} for CA, Gd-CA-1, Gd-CA-2, and Gd-CA-3, respectively.

Fig. 1f shows the XRD patterns for all samples. For CAs, a broad peak corresponding to the (002) plane indicates their amorphous carbon nature. For all Gd-CA samples, a distinct graphite phase diffraction peak at approximately 25° emerges, indicating a high degree of reduction of the graphene-drums during the thermal annealing process. Raman spectroscopy results in Fig. 1g further elucidate the carbon phase structures of Gd-CAs. The presence of two broad peaks at 1346 cm^{-1} (D-band) and 1589 cm^{-1} (G-band) in all samples verifies the existence of defective carbon and crystallized graphite.[21] CAs exhibit two non-sharp peaks of the D and G bands, indicating their amorphous carbon nature.[22] The incorporation of graphene-drums in Gd-CAs enhances the intensities of the D and G bands and results in an increased intensity ratio of I_D/I_G, suggesting an increased amount of defective graphene introduced into the Gd-CAs as the quantity of graphene-drums grew. Additionally, the emergence of the 2D band and the D + D′ combination mode in Gd-CA-2 and Gd-CA-3 samples signifies the presence of both monolayer and multilayers of graphene nanosheets.[23]

2.2 Mechanical robustness of Gd-CAs

The robust mechanical strength of Gd-CAs is essential for their practical applications. Fig. 2a–d display the compressive stress–strain (σ–ε) curves of CA and Gd-CAs under increasing strains of 40%, 60%, and 80%. Notably, all samples exhibit closed loops in the σ–ε curves under varied strains, indicating their ability to return to their original state after undergoing substantial deformation of up to 80% strain. Among the samples, CA displays the lowest compressive stress at 80% strain of only 43 kPa. Fig. 2b–d reveal an increase in the mechanical strength of Gd-CAs from 83 kPa for Gd-CA-1, to 150 kPa for Gd-CA-2, and 205 kPa for Gd-CA-3 at 80% compression strain. Fig. 2e summarizes and highlights the improvement in compression stress at 80% strain of all samples with the increase of
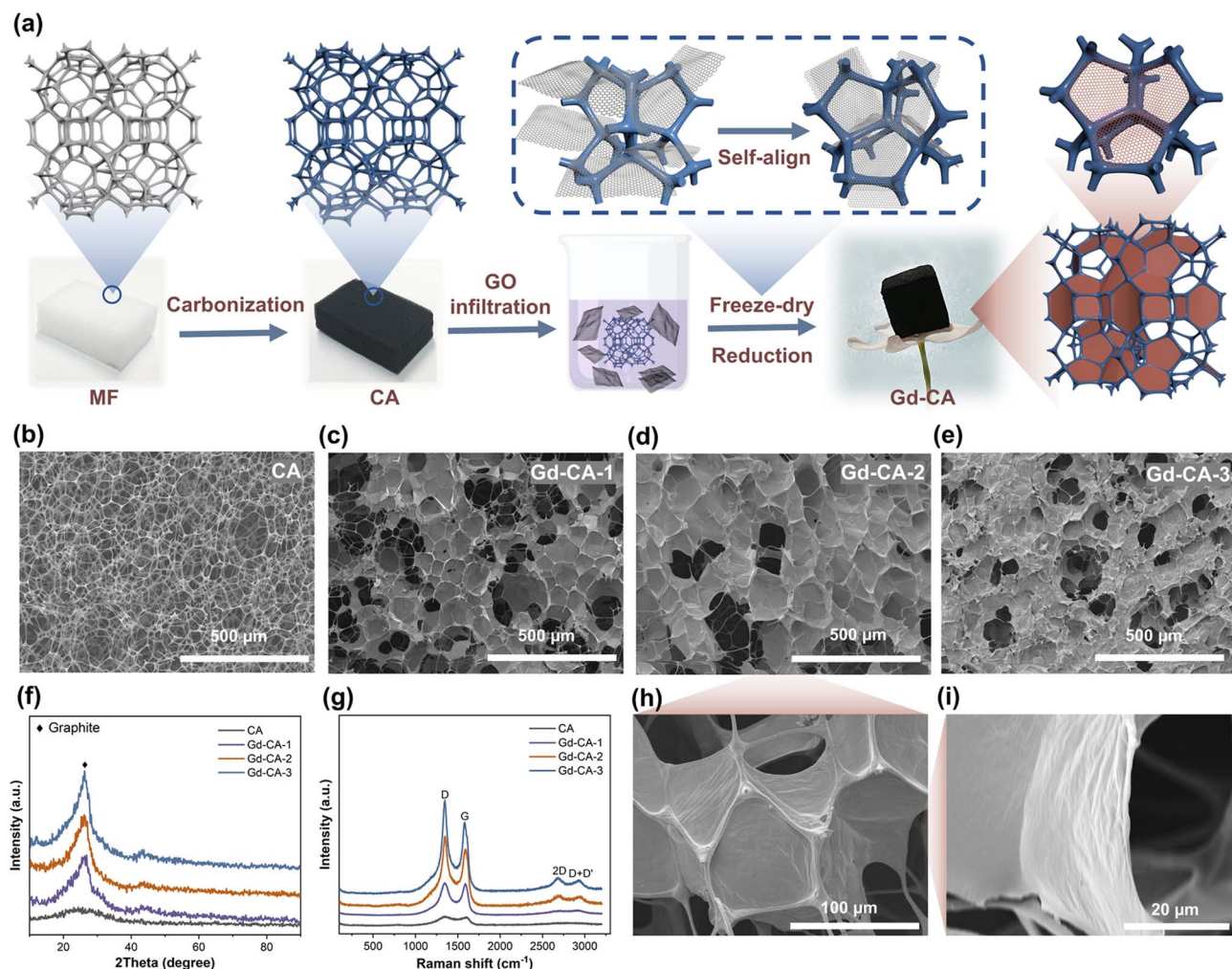
This journal is © The Royal Society of Chemistry 2023

J. Mater. Chem. A, 2023, **11**, 23452–23462 | **23453**

Fig. 1 (a) Illustration of the fabrication process of Gd-CAs. SEM images of (b) CA, (c) Gd-CA-1, (d) Gd-CA-2, and (e) Gd-CA-3. (f) XRD pattern and (g) Raman spectra of CA and Gd-CAs. (h) and (i) SEM images of Gd-CA-2.

graphene-drums in CAs. Additionally, cyclic compression test results reveal that Gd-CA-2 retains 90% of its original compressive stress even after the 1000th cycle (Fig. 2f), showcasing its excellent fatigue resistance. Furthermore, Fig. 2g illustrates the structural integrity of the sample Gd-CA-2 even after severe compression deformation and high pressure and tension exposure, indicating its structural reliability. The exceptional resilience and robustness of Gd-CAs can be attributed to the synergistic effects of the CA skeleton support and graphene-drum strengthening through the edge-to-edge connections. As depicted in Fig. 2h, though the porous structure of CA offers significant compressible space, their thin and long trusses are prone to breaking under large deformations. Coincidentally, without the strut skeleton support, the graphene sheets cannot self-support and are susceptible to slipping under compression due to weak Van der Waals bonding. By incorporating graphene-drums to connect the carbon strut skeletons, the graphene-drums across the CA trusses provide additional paths to distribute external forces, preventing the breaking of the struts and fracturing of the skeletons during

compression. Simultaneously, the carbon skeletons provide continuous interconnected support to the graphene-drums, preventing them from collapsing and slipping under deformation. Thus, the unique combination of continuous carbon truss support and graphene-drum strengthening enhances the robustness and resilience of Gd-CAs.

2.3 Acoustic wave absorption performance of Gd-CAs

The sound absorption test was conducted based on the ASTM E2611-17 standard for CA and Gd-CA samples at different thicknesses (10 mm, 20 mm, and 30 mm) (Fig. 3a–c).[24] The CA exhibited typical flexible open cell structure behavior, with the absorption coefficient increasing linearly with frequency at low thickness (10 mm), and additional shearing resonances were observed for the thicker samples (20 mm and 30 mm). With the addition of graphene-drums, there is a significant improvement in the acoustic absorption performance of all Gd-CA samples across all thicknesses. At the same time, all the absorption peaks shift towards lower frequencies with increasing graphene-drum content, indicating that Gd-CAs are more
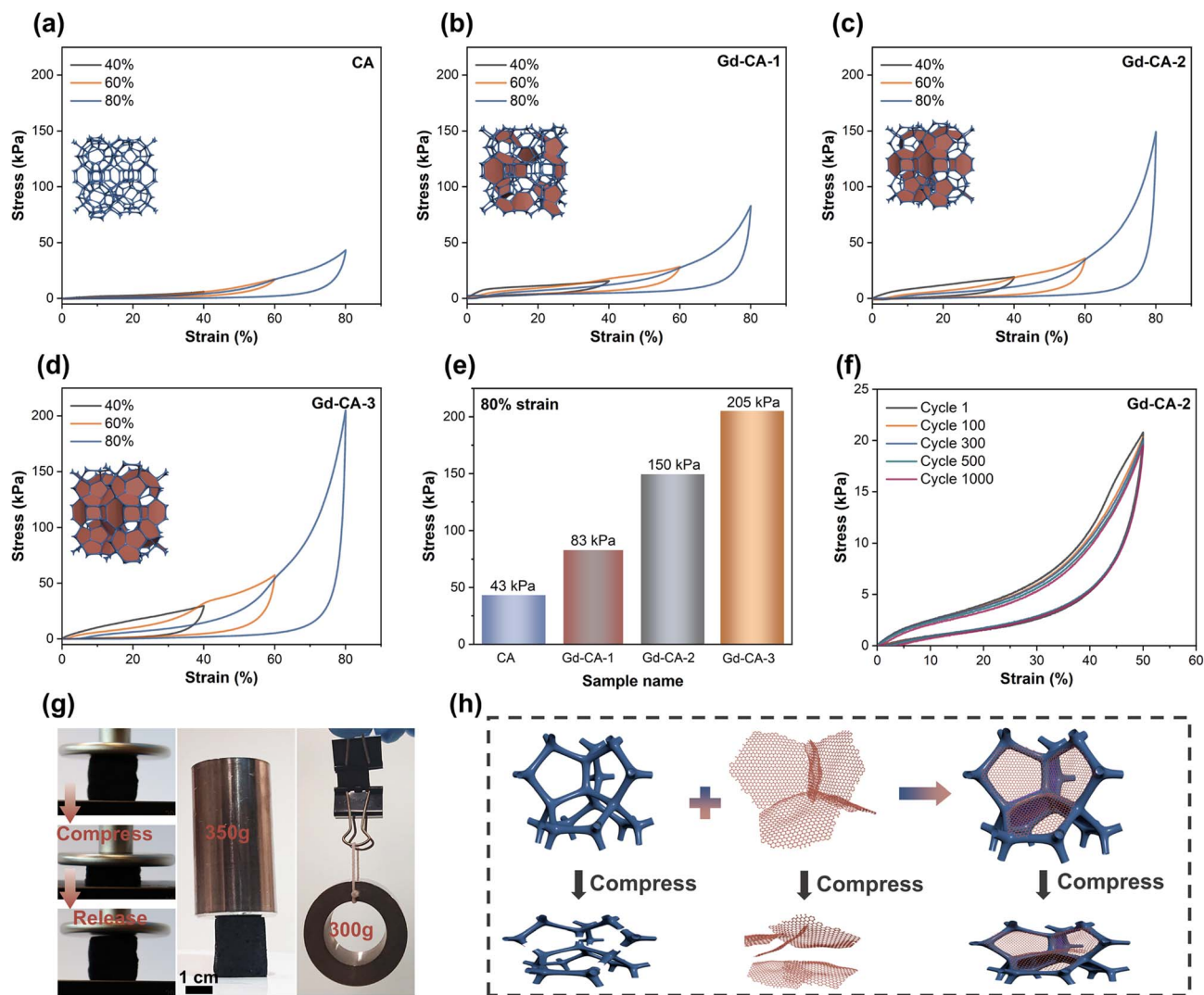
23454 | *J. Mater. Chem. A*, 2023, **11**, 23452–23462

This journal is © The Royal Society of Chemistry 2023

View Article Online
Paper

Journal of Materials Chemistry A

Open Access Article. Published on 13 October 2023. Downloaded on 1/14/2026 5:30:39 PM. This article is licensed under a Creative Commons Attribution-NonCommercial 3.0 Unported Licence.

Fig. 2 The compressive stress–strain (σ–ε) curves of (a) CA, (b) Gd-CA-1, (c) Gd-CA-2, and (d) Gd-CA-3 at different compression strains. (e) The comparison of stress of CA and Gd-CAs at 80% compression strain. (f) The cyclic compressive σ–ε curves of Gd-CA-2 at 50% strain. (g) Image showing the excellent resilience and resistance to compressive and tensile strength of the sample Gd-CA-2. (h) Schematic diagram showing the compressive deformation mechanism of the Gd-CAs.

effective in absorbing low-frequency broadband signals. However, the absorption coefficients of Gd-CA-3 showed a slight increase compared to Gd-CA-2, indicating saturation of absorption as the graphene-drum infiltration content increased, primarily due to the overlapping and thickening of graphene sheets suppressing resonance absorption.[25] Specifically, we compared the absorption coefficient of the sample Gd-CA-2 at different thicknesses as shown in Fig. 3d. The 10 mm sample primarily exhibited high-frequency acoustic absorption dominated by friction damping. Increasing the thickness to 20 mm introduced an additional low-frequency resonance peak, with an absorption coefficient exceeding 0.8 between 800 and 1500 Hz and nearly reaching 1 around 1000 Hz. Further thickness increases to 30 mm shifted the first resonance peak to even lower frequencies, with an absorption coefficient exceeding 0.8 between 500 and 1000 Hz. The second peak also broadened, maintaining an absorption coefficient above 0.8 across the

frequency band of 1500–6300 Hz. These two wide absorption peaks in Gd-CA-2 indicate its capability for broadband absorption that enables the dissipation of common noises encountered in daily life, traffic, and industry. The noise reduction coefficient (NRC) was calculated for all samples by averaging the sound absorption coefficients at 250, 500, 1000, and 2000 Hz (Fig. 3e). The NRC values of Gd-CAs consistently increased with higher graphene-drum contents at any given thickness. At a 30 mm thickness, Gd-CA-2 and Gd-CA-3 achieved a NRC of 0.59 and 0.67, respectively, showcasing significant enhancements compared to CA (0.36). Moreover, they outperformed most of the recently developed lightweight porous noise-absorbing materials, including polymer foams,[26,27] fibrous materials,[27–29] and graphene-based materials,[26,30–37] thereby confirming their superiority (Fig. 3f and Table S1†).

The superior acoustic absorption ability of Gd-CAs can be primarily attributed to the improved air-flow resistance

This journal is © The Royal Society of Chemistry 2023

J. Mater. Chem. A, 2023, **11**, 23452–23462 | **23455**
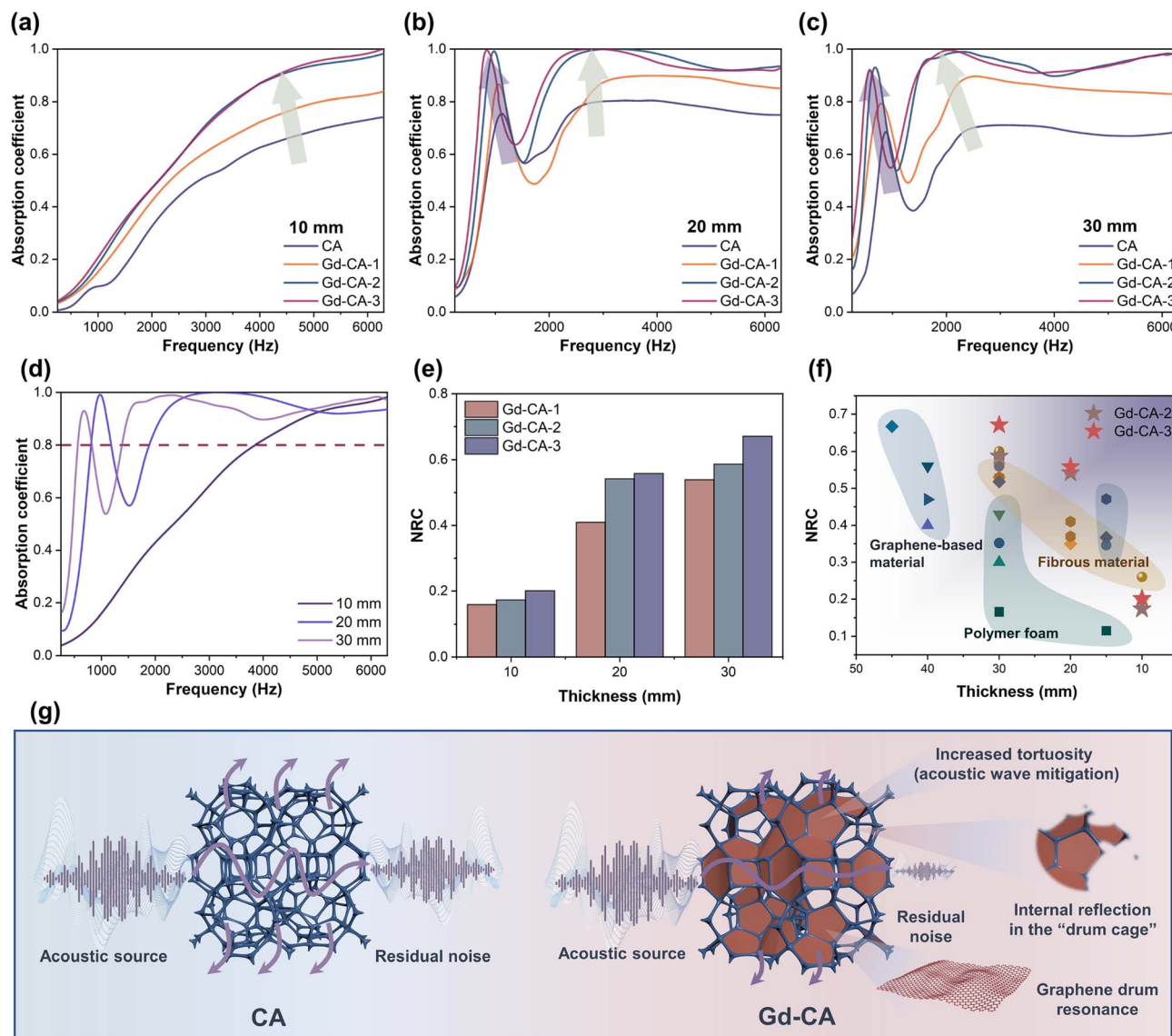

Fig. 3 Acoustic absorption coefficients of CA and Gd-CAs at a thickness of (a) 10 mm, (b) 20 mm, and (c) 30 mm. (d) Thickness dependent acoustic absorption of Gd-CA-2. (e) Comparison of the NRC value of Gd-CAs at different thicknesses. (f) Comparison of the NRC between Gd-CAs and other reported porous acoustic absorption materials with different thicknesses. (g) Schematic illustration of the acoustic absorption mechanism of Gd-CAs.

facilitated by the interconnected graphene-drums bridging across the trusses. Fig. 3g illustrates that the fully open cell strut connected framework of CA provides only weak air-flow resistance due to its high porosity and limited tortuous paths. In contrast, the interconnected graphene-drums within the CA skeleton encompass numerous pores, elongating the wave propagation path and significantly increasing energy mitigation tortuosity. Moreover, the edge-to-edge arranged graphene-drums form interconnected cell walls resembling "cages", impeding the escape of acoustic waves and promoting effective energy dissipation through internal reflections. Additionally, the thin graphene-drum-induced resonance contributes to additional damping and friction loss, further dissipating energy.[9,38] As a result, the Gd-CAs in this study exhibit multiple loss mechanisms combined with porous structural air-flow

resistance and graphene-drum damping resonance, leading to enhanced broadband acoustic absorption.

2.4 Electromagnetic wave (EMW) attenuation performance of Gd-CAs

The electromagnetic parameters of all samples, including the real (ε') and imaginary (ε'') parts of permittivity, were measured across a frequency range of 2 to 18 GHz. Generally, ε' indicates the material's ability to store electromagnetic energy, while ε'' represents its energy attenuation capability.[39] Fig. 4a and b illustrate the frequency-dependent variations of ε' and ε'' for CA and Gd-CAs. Both ε' and ε'' of CA remain consistently low throughout the tested frequency band. As graphene-drums increase, the complex permittivity of Gd-CAs demonstrates an upward trend
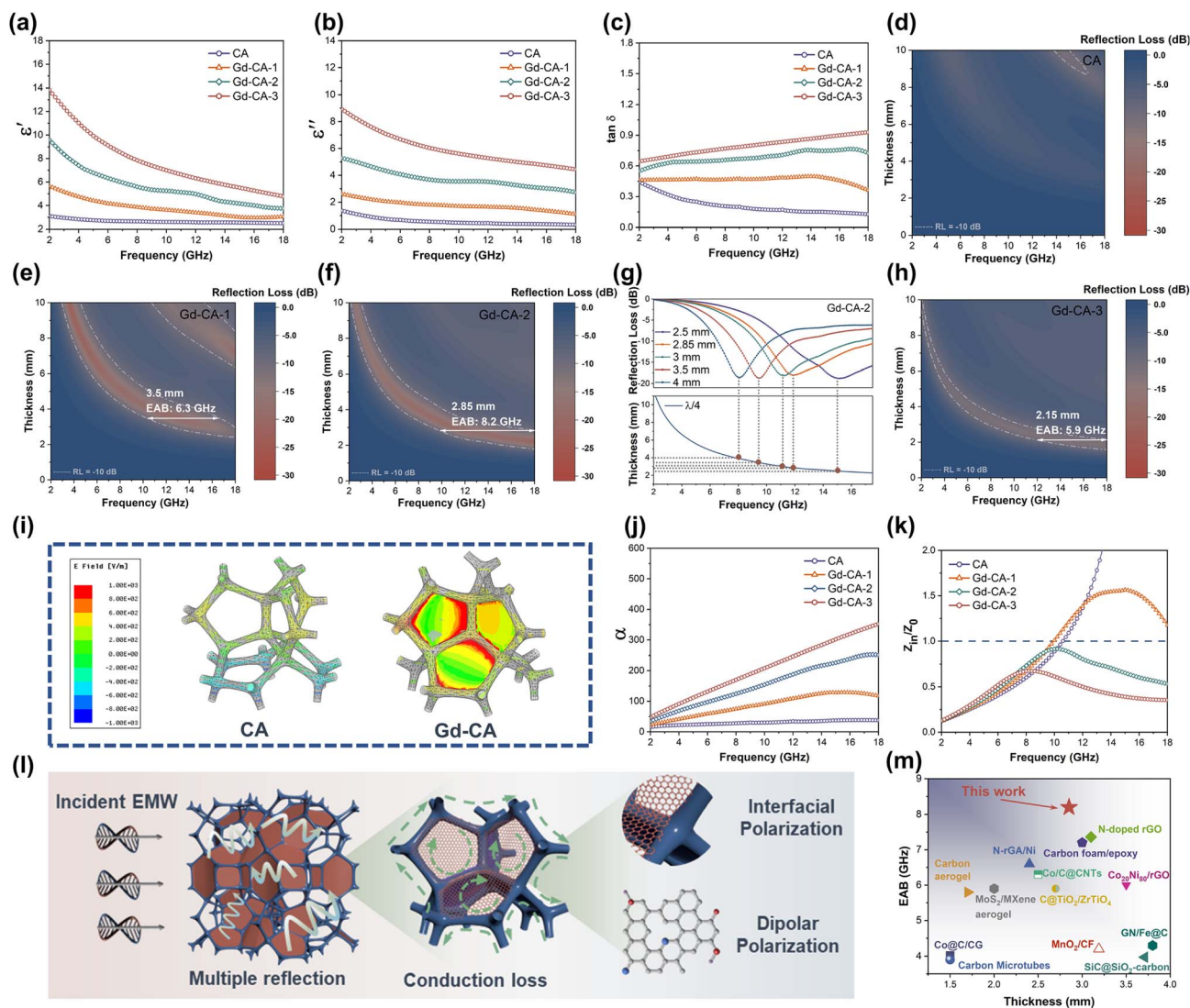
23456 | J. Mater. Chem. A, 2023, 11, 23452–23462

This journal is © The Royal Society of Chemistry 2023

Fig. 4 The electromagnetic parameters including (a) ε', (b) ε'', and (c) and $\tan\delta$ for CA and Gd-CAs. Reflection loss 3D plots of (d) CA, (e) Gd-CA-1, (f) Gd-CA-2, and (h) Gd-CA-3. (g) The RL value curves and matching thickness *versus* peak frequency of Gd-CA-2 in the $\lambda/4$ model. (i) Simulated electric power loss distribution of CA and Gd-CAs under an electromagnetic field. (j) The attenuation constant (α) and (k) impedance matching degree of CA and Gd-CAs. (l) Schematic diagram of the EMW attenuation mechanism of Gd-CAs. (m) EAB comparison of Gd-CA-2 with reported carbon-based porous materials.

from Gd-CA-1, Gd-CA-2 to Gd-CA-3. Concurrently, the electrical conductivity of Gd-CAs improves with the increase of the graphene-drum incorporation content. In comparison to the low conductivity of 1.37 S m^{-1} for CAs, Gd-CAs exhibit higher values of 2.96 S m^{-1}, 4.31 S m^{-1}, and 6.35 S m^{-1} for Gd-CA-1, Gd-CA-2, and Gd-CA-3, respectively (Fig. S3†). This suggests the formation of more conduction paths as graphene-drums bridge across the carbon trusses, potentially enhancing conductive loss. Simultaneously, an enhanced frequency dispersion of permittivity is observed, characterized by a noticeable decrease in permittivity with increasing frequency. This improved frequency dispersion, resulting from enhanced conductive loss and interface polarization in Gd-CAs, lays the foundation for potential broadband EMW attenuation.[40] The dielectric loss tangent ($\tan\delta_\varepsilon = \varepsilon''/\varepsilon'$), depicted in Fig. 4c, is utilized to express the inherent EMW dissipation capability of materials.[41] It exhibits an increasing trend from CA

to Gd-CAs, aligning with the complex permittivity, thereby further confirming the enhanced dielectric loss ability of Gd-CAs. As the dielectric EMW attenuators, the incident electromagnetic energies are prominent and dissipated by the dielectric loss, including conductive and polarization loss.[42] Thus, it can be inferred that the Gd-CAs may have enhanced EMW attenuation performance compared to that of CAs.

Based on transmission line theory and the metal back-panel model to eliminate the transmission of EMWs through the material, the reflection loss (RL) of all samples was calculated as a direct measure of their EMW attenuation performance.[43,44] The effective attenuation bandwidth (EAB), defined as RL < −10 dB (90% absorption), serves as a critical determinant of the efficiency of broadband EMW attenuators. The detailed calculation equation is given in eqn (S1), (S2) and Section S2, ESI.† Fig. 4d–f and h depict the continuous variation of RL values

with frequency for CA and Gd-CAs across a thickness range of 0–10 mm. As expected, CA exhibits a narrow EAB when the thickness exceeds 8.2 mm (Fig. 4d). With the incorporation of graphene-drums, Gd-CA-1 demonstrates an EAB of 6.3 GHz at a thickness of 3.5 mm (Fig. 4e). Upon further increasing the graphene-drum contents, Gd-CA-2 exhibits enhanced broadband EMW attenuation capability with an EAB of 8.2 GHz at a reduced thickness of 2.85 mm (Fig. 4f). Besides, Fig. S4† highlights that Gd-CA-2 maintains a high EAB value in the thickness range of 2.5–3.0 mm, further emphasizing its efficient broadband dissipation ability for EMW energies. Meanwhile, Gd-CA-2 achieves a minimum RL of −18 dB at 11.9 GHz with a thickness of 2.85 mm, aligning with the quarter-wavelength ($\lambda/4$) cancellation law.[17] This model establishes a relationship between the matching thickness (t_m) and the corresponding matching frequency (f_m), defined by the following equation:

$$t_m = n\lambda/4 = nc/4f_m\sqrt{\mu_r\varepsilon_r} \quad (n = 1, \ 3, \ 5...) \tag{1}$$

where λ is the quarter-wavelength at f_m, c is the velocity of light, and ε_r and μ_r are the complex permittivity and the permeability, respectively. When the sample thickness aligns with odd multiples of $\lambda/4$, sharp destructive interference occurs between the incident and reflected EMWs, resulting in the lowest RL values. Fig. 4g illustrates the relationship between f_m and t_m at $\lambda/4$ wavelengths for Gd-CA-2. The lowest RL peaks for Gd-CA-2 align well with the $\lambda/4$ model at various thicknesses, offering an explanation for the occurrence of the lowest RL peaks at specific frequencies and thicknesses. However, excessive graphene-drum content in Gd-CA-3 results in a narrowed EAB of 5.9 GHz at a thickness of 2.15 mm (Fig. 4h).

This phenomenon can be explained by an imbalance between the attenuation constant (α) and impedance matching degree ($|Z_{in}/Z_0|$).[45,46] By eqn (2), the α value of all the samples is calculated and shown in Fig. 4j, which represents the inner capacity to dissipate EMWs and a larger α indicates a higher dissipation ability.

$$\alpha = \frac{\sqrt{2}\pi f}{c} \times \sqrt{(\mu''\varepsilon'' - \mu'\varepsilon') + \sqrt{(\mu''\varepsilon'' - \mu'\varepsilon')^2 + (\mu''\varepsilon'' + \mu'\varepsilon')^2}} \tag{2}$$

where c is the light speed in vacuum. μ' and μ''' are equal to 1 and 0, respectively, for non-magnetic materials. Among all the samples, the attenuation constant (α) follows a similar trend to the $\tan\delta_\varepsilon$ values, indicating their attenuation capabilities of EMWs. CA exhibits weak EMW dissipation, while Gd-CAs demonstrate gradually enhanced attenuation capacity with the increase of graphene-drums. Fig. 4k illustrates the $|Z_{in}/Z_0|$ values of all samples at a thickness of 2.85 mm, which determine the extent to which incident EMWs can penetrate the attenuator from free space. Ideal impedance matching occurs when $|Z_{in}/Z_0|$ approaches 1, indicating full EMW penetration into the materials. CA, Gd-CA-1, and Gd-CA-3 exhibit either excessive or insufficient $|Z_{in}/Z_0|$ values across the frequency range, indicating a strong impedance mismatch between EMWs and the aerogel surface. Therefore, although Gd-CA-3 possesses a high attenuation constant, the imperfect impedance ratio

diminishes its EMW attenuation efficiency. In contrast, Gd-CA-2 achieves optimal impedance matching from 10–18 GHz, with $|Z_{in}/Z_0|$ approaching 1. Therefore, the synergistic effects of a high attenuation constant and ideal impedance matching ensure maximum EMW penetration into Gd-CA-2, facilitating efficient subsequent dissipation and resulting in optimal EMW attenuation performance.

To visually demonstrate the improved electromagnetic power loss in Gd-CAs, finite element simulations were conducted using HFSS software (Fig. 4i). For simplicity, the simulation model comprised four carbon truss cell units with and without graphene-drums. The detailed simulation method is provided in Section S2, ESI.† The results indicate that although conductive pathways exist in CA, the overall electrical power loss remains insufficient due to the strut-connected open cell network. Upon the graphene-drum bridging, the Gd-CA units exhibit significantly enhanced electric loss volume and intensity when exposed to an alternating electromagnetic field. This is mainly attributed to the improved dielectric losses and interfacial polarization provided by the increased conductive pathways and micro–nano-level interfaces of interconnected graphene-drums. Considering the aforementioned findings, Fig. 4l summarizes the overall EMW attenuation mechanism of Gd-CAs as follows: (i) impedance matching allows most incident EMWs to enter Gd-CAs, reducing reflection. Subsequently, multiple random reflections occur at the internal interfaces of the drum walls, consuming electromagnetic energy. (ii) Bridged graphene-drums form continuous pathways for electron migration, facilitating conduction loss. (iii) Rich heterointerfaces between graphene-drums and carbon skeletons amplify interfacial polarization loss. Meanwhile, dipolar polarization from open edges and in-plane defects of thermally reduced graphene-drums enhances energy storage and EMW attenuation. Additionally, the $\lambda/4$ cancelation occurs at the matched thickness, resulting in the strongest attenuation at the specified thickness and frequency. In conclusion, Gd-CAs effectively capture and attenuate incident EMW energy through impedance matching, multiple internal reflections, conduction loss, polarization relaxation loss, and $\lambda/4$ cancelation, making them highly efficient broadband EMW attenuators. Fig. 4m and Table S2† summarize the EMW attenuation performance of typical carbon-based porous materials reported in recent literature.[47-59] Gd-CA-2 achieves a superior broadband EAB with a thinner thickness compared to similar studies, highlighting its exceptional efficiency as an EMW attenuator.

EMW attenuation materials with a broadband EAB and high conductivity are highly promising for low-reflection EMW shielding applications. Considering EMW transmission through materials, the reflection (R), absorption (A), and transmission (T) coefficients, as well as the EMW shielding efficiency (SE), encompassing total (SE_T), reflection (SE_R), and absorption (SE_A) shielding efficiency for both CAs and Gd-CAs were calculated using eqn (S3)–(S9), Section S2, ESI.† The results presented in Fig. S5† demonstrate an increase in R and A coefficients and a decrease in T coefficients due to enhanced graphene-drum incorporation, at a specified sample thickness of 2.85 mm. This signifies more EMWs being reflected and attenuated within the Gd-CAs with increased graphene-drum content. Accordingly, the

23458 | J. Mater. Chem. A, 2023, 11, 23452–23462

This journal is © The Royal Society of Chemistry 2023

SE_T, SE_R, and SE_A exhibit a consistent increasing trend with enhanced graphene-drum incorporation. Notably, SE_A values increase more than SE_R values, suggesting an augmented absorption-domain shielding mechanism (Fig. S6†). However, at a thin thickness of 2.85 mm, the total SE_T does not surpass 10 dB for Gd-CAs. Therefore, we proceeded to calculate the R, T, and A coefficients, as well as SE values for Gd-CA-2 at a thickness of 10 mm, to further explore its potential for low-reflection EMW shielding performance. As depicted in Fig. S7a,† the A coefficient significantly surpasses R and T values across the tested frequency band, indicating a low reflection/transmission shielding mechanism. Moreover, the SE_A value closely matches SE_T and exceeds 20 dB at high frequencies, demonstrating excellent absorption-domain shielding effectiveness (Fig. S7b†). Hence, the application of Gd-CAs holds great promise for extending to low-reflection EMW shielding applications.

2.5 Multifunction integration of Gd-CAs and their potential applications

For practical application, multifunctional integration is necessary for maintaining consistent performance. Waterproofing capabilities are crucial, especially for outdoor applications as EMW attenuators and acoustic absorbers. Due to their porous structures, materials like CAs are especially prone to absorb moisture, which leads to weight increase and loss of operational efficiency (Fig. S8†). However, the sample Gd-CA-2 exhibits a significantly enhanced water contact angle of approximately 120°, indicating excellent hydrophobicity (Fig. 5a). This is due to the interconnected graphene-drums creating impermeable barrier layers against moisture penetration. Fire retardancy is also a fundamental requirement for practical applications. Fig. 5a shows that even after 30 s of flame exposure, the Gd-CA-2
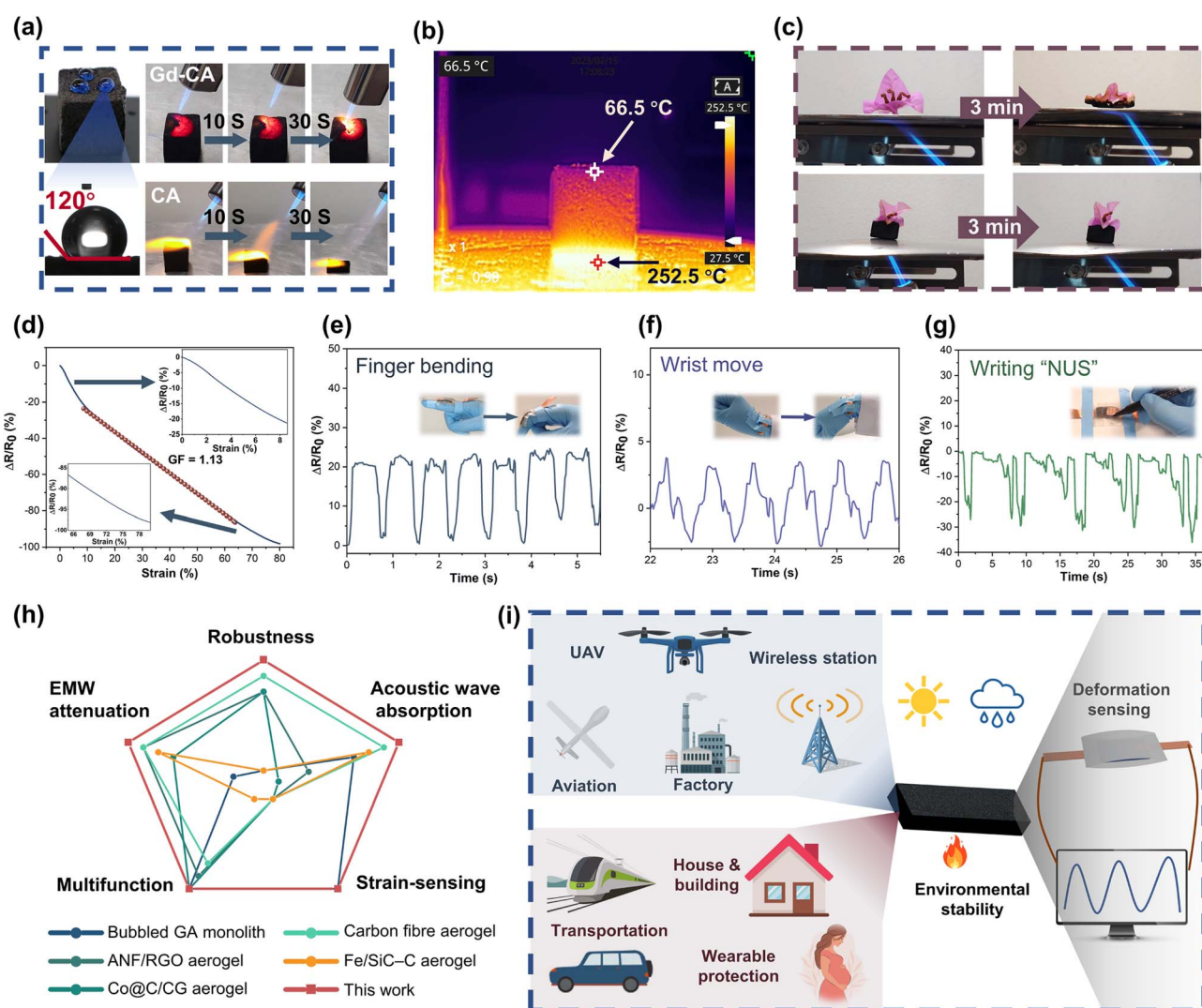

Fig. 5 (a) Photographs of water droplets on the surface of the sample Gd-CA-2, the water contact angle of Gd-CA-2, and digital photographs of the burning test. (b) Infrared thermal images of Gd-CA-2 on a heating plate at 250 °C. (c) Digital photographs of the flowers with or without Gd-CA-2 thermal insulation when heated with a flame gun. (d) $\Delta R/R_0$ of Gd-CA-2 as a function of compression strain. Sensing performance of Gd-CA-2 for real-time detection of (e) finger bending, (f) wrist movement, and (g) writing. (h) Radar chart for the overall appreciation of the Gd-CAs compared with other carbon-based porous materials. (i) Illustration of the potential applications of the Gd-CAs, for use in the elimination of wave pollution in the fields of aviation, engineering, transportation, household, personal protection, and deformation monitoring.

This journal is © The Royal Society of Chemistry 2023

J. Mater. Chem. A, 2023, **11**, 23452–23462 | **23459**

sample retains stable structure integrity, indicating superior fire retardancy. These exceptional fire-retardant properties of Gd-CAs stem from their 3D interconnected porous graphene-based structure, which prevents the formation of carbonyl defects and enables the trapping of nonflammable carbon dioxide gas within the pores.[60] In contrast, the CA sample quickly burned out, displaying noticeable blazing flames within 30 s of exposure to the fire source. Additionally, Gd-CAs exhibit promising thermal insulation due to their porous microstructures. Despite graphene being highly thermally conductive, Gd-CAs maintain exceptionally low thermal conductivity owing to their porous structure with a minimal solid phase volume.[61] In comparison to fully open-cell structured CAs, characterized by a low thermal conductivity of 0.018 W m^{-1} K^{-1} due to a significant volume of air, the thermal conductivity of Gd-CAs shows a negligible increase upon graphene-drum incorporation (Fig. S9†). Specifically, Gd-CA-2 displays a low thermal conductivity of 0.025 W m^{-1} K^{-1}. Even at the highest graphene-drum content in Gd-CA-3, this value does not exceed 0.026 W m^{-1} K^{-1}, surpassing the thermal conductivity of most commercial thermal insulators (Fig. S9†).[62] As demonstrated in Fig. 5b, after 30 minutes on a 250 °C heating platform, the top surface of a 20 mm thick Gd-CA-2 sample only reaches 66.5 °C, with a substantial temperature difference of approximately 183.5 °C, showcasing its superior thermal insulation performance to even keep the flower fresh above a flame gun (Fig. 5c).

In industries such as aerospace, transportation, and factories where real-time monitoring is challenging, the self-sensing abilities of Gd-CAs are particularly beneficial. The strain-sensing performance of Gd-CA-2 was evaluated by connecting it to an impedance meter to measure the relative resistance change ($\Delta R/R_0 = (R - R_0)/R_0$, where R and R_0 represent instantaneous resistance and initial resistance, respectively) under different strains. Fig. 5d presents the resistance variation of Gd-CA-2 with compression strain increases up to 90%. A highly linear relationship between resistance variation and compression strain is observed, which has a gauge factor (GF) of 1.13. Furthermore, the real-time sensing ability of Gd-CA-2 was assessed by attaching the Gd-CA sensor to various parts of the human body. As depicted in Fig. 5e, f and S10b–d,† the sensor exhibits stable and reproducible real-time sensing signals in response to repetitive finger bending, wrist moving, twisting, throat, and joint motions. Additionally, by writing on the sensor surface, characters such as "NUS" can be clearly identified, as shown in Fig. 5g. These results demonstrate the consistent and accurate conversion of deformation signals generated by human motion into electrical signals through resistance change. Fig. 5h provides a comprehensive assessment of Gd-CAs by comparing them with newly reported graphene/carbon-based porous materials in terms of wave pollution attenuation, functionality, and practical applications.[32,35,39,63,64] The evaluation considers five key metrics: robustness, EMW attenuation, acoustic wave absorption, multifunction, and strain-sensing performance. The benchmarks for these comparisons are specified in Table S3.† The results unequivocally demonstrate that Gd-CAs outperform other graphene/carbon-based materials in all five criteria, highlighting

their remarkable potential for practical applications requiring dual-wave attenuation.

Fig. 5i explores the diverse application potential of Gd-CAs in various sectors. The Gd-CAs offer a versatile solution to mitigate both acoustic and electromagnetic pollution produced by diverse engineering facilities, including aviation, aircraft, factories, and wireless stations. Considering the practical application, Gd-CAs demonstrate adaptability to extreme temperature and moisture environments. They can also be used as filling materials for wearable clothing, safeguarding individuals against the adverse effects of noise and electromagnetic waves. Furthermore, the strain-sensing capabilities of Gd-CA attenuators enable them to function as self-monitoring devices. By monitoring the resistance signal variation resulting from the deformation of Gd-CA attenuators, immediate feedback can be obtained when external forces impact the attenuators. This feature is particularly valuable for monitoring the deformation of Gd-CA attenuators in unmanned areas.

3. Conclusions

In summary, this study successfully developed graphene-drum bridged carbon aerogels (Gd-CAs), with an interconnected graphene-drum bridged carbon truss microstructure. The binary interaction between the graphene-drum and carbon skeleton leads to high robustness and structural stability of Gd-CA-2, capable of withstanding compression stress up to 150 kPa at 80% strain and exhibiting excellent compression fatigue resistance (1000 cycles at 50% strain). The unique porous cell microstructure, equipped with interconnected thin graphene drums, facilitated the synergistic dissipation of acoustic energy through enhanced air-flow resistance and drum resonance dissipation. Gd-CA-2 demonstrated a significantly improved engineering noise reduction coefficient of 0.55. Additionally, by balancing impedance matching and dielectric loss, Gd-CA-2 could effectively capture and attenuate incident electromagnetic wave energy, resulting in an impressive effective broad attenuation bandwidth of 8.2 GHz at a thickness of 2.8 mm. Moreover, the multiscale porous conductive architecture of Gd-CAs endowed them with multiple functional properties, including waterproofing, nonflammability, thermal insulation, and strain-sensing. These properties ensure the durability and adaptability of the attenuator in various environments. Consequently, the Gd-CA attenuator presents an effective strategy for addressing the urgent need to mitigate acoustic and electromagnetic pollution, with great potential for application in aviation, aerospace, and other civil and engineering sectors.

4. Experimental

All experimental procedures are given in the ESI.†

Author contributions

Y. Zhao: conceptualization, methodology, investigation, writing – original draft, and writing – review and editing. T. Niu: methodology, validation, and data curation. X. Dong:

23460 | *J. Mater. Chem. A*, 2023, **11**, 23452–23462

This journal is © The Royal Society of Chemistry 2023

Conflicts of interest

There are no conflicts to declare.

Acknowledgements

References

1 M. S. Thomas Münzel, F. Schmidt, E. Schmidt, S. Steven, S. Kröller-Schön and A. Daiber, *Antioxid. Redox Signaling*, 2018, **28**, 873–908.

2 F. Shahzad, M. Alhabeb, C. B. Hatter, B. Anasori, S. Man Hong, C. M. Koo and Y. Gogotsi, *Science*, 2016, **353**, 1137–1140.

3 H. Ge, M. Yang, C. Ma, M. H. Lu, Y. F. Chen, N. Fang and P. Sheng, *Natl. Sci. Rev.*, 2018, **5**, 159–182.

4 D. Zong, L. Cao, Y. Xin, Y. Si, S. Zhang, J. Yu and B. Ding, *Nat. Commun.*, 2021, **12**, 6599.

5 M. Qin, L. Zhang and H. Wu, *Adv. Sci.*, 2022, **9**, 2105553.

6 L. Liang, Q. Li, X. Yan, Y. Feng, Y. Wang, H.-B. Zhang, X. Zhou, C. Liu, C. Shen and X. Xie, *ACS Nano*, 2021, **15**, 6622–6632.

7 M. Rapisarda, G. P. M. Fierro and M. Meo, *Sci. Rep.*, 2021, **11**, 10572.

8 R. De Alba, F. Massel, I. R. Storch, T. S. Abhilash, A. Hui, P. L. McEuen, H. G. Craighead and J. M. Parpia, *Nat. Nanotechnol.*, 2016, **11**, 741–746.

9 K. Pang, X. Liu, J. Pang, A. Samy, J. Xie, Y. Liu, L. Peng, Z. Xu and C. Gao, *Adv. Mater.*, 2022, **34**, 2103740.

10 C. Simón-Herrero, N. Peco, A. Romero, J. L. Valverde and L. Sánchez-Silva, *Applied Acoustics*, 2019, **156**, 40–45.

11 L. Liu, Y. J. Chen, H. Z. Liu, H. U. Rehman, C. Chen, H. M. Kang and H. Li, *Soft Matter*, 2019, **15**, 2269–2276.

12 M. J. Nine, M. Ayub, A. C. Zander, D. N. H. Tran, B. S. Cazzolato and D. Losic, *Adv. Funct. Mater.*, 2017, **27**, 1703820.

13 J. Lee and I. Jung, *Applied Acoustics*, 2019, **151**, 10–21.

14 M. Rapisarda, G.-P. Malfense Fierro and M. Meo, *Sci. Rep.*, 2021, **11**, 10572.

15 B. Lu, L. Lv, H. Yang, J. Gao, T. Xu, G. Sun, X. Jin, C. Shao, L. Qu and J. Yang, *J. Mater. Chem. A*, 2019, **7**, 11423–11429.

16 X. Huang, G. Yu, Y. Zhang, M. Zhang and G. Shao, *Chem. Eng. J.*, 2021, **426**, 131894.

17 R. Shu, G. Zhang, C. Zhang, Y. Wu and J. Zhang, *Adv. Electron. Mater.*, 2021, **7**, 2001001.

18 W. Huang, X. Zhang, J. Chen, Q. Qiu, Y. Kang, K. Pei, S. Zuo, J. Zhang and R. Che, *Adv. Sci.*, 2023, 2303217.

19 Y. Li, F. Meng, Y. Mei, H. Wang, Y. Guo, Y. Wang, F. Peng, F. Huang and Z. Zhou, *Chem. Eng. J.*, 2020, **391**, 123512.

20 C. Li, D. Jiang, H. Liang, B. Huo, C. Liu, W. Yang and J. Liu, *Adv. Funct. Mater.*, 2018, **28**, 1704674.

21 Z. Li, L. Deng, I. A. Kinloch and R. J. Young, *Prog. Mater. Sci.*, 2023, **135**, 101089.

22 J.-B. Wu, M.-L. Lin, X. Cong, H.-N. Liu and P.-H. Tan, *Chem. Soc. Rev.*, 2018, **47**, 1822–1873.

23 A. C. Ferrari and D. M. Basko, *Nat. Nanotechnol.*, 2013, **8**, 235–246.

24 X. W. Li, X. Yu and W. Zhai, *Adv. Mater.*, 2021, **33**, 2104552.

25 X. He, S. Kitipornchai and K. Liew, *Nanotechnology*, 2005, **16**, 2086.

26 J. H. Oh, H. R. Lee, S. Umrao, Y. J. Kang and I. K. Oh, *Carbon*, 2019, **147**, 510–518.

27 L. T. Cao, Y. Si, Y. Y. Wu, X. Q. Wang, J. Y. Yu and B. Ding, *Nanoscale*, 2019, **11**, 2289–2298.

28 Y. Feng, D. Zong, Y. Hou, X. Yin, S. Zhang, L. Duan, Y. Si, Y. Jia and B. Ding, *J. Colloid Interface Sci.*, 2021, **593**, 59–66.

29 Y. Xie, L. Wang, Y. Peng, D. Ma, L. Zhu, G. Zhang and X. Wang, *Chem. Eng. J.*, 2021, **416**, 128994.

30 K. Pang, X. T. Liu, J. T. Pang, A. Samy, J. Xie, Y. J. Liu, L. Peng, Z. Xu and C. Gao, *Adv. Mater.*, 2022, **34**, 2103740.

31 D. D. Zong, L. T. Cao, X. Yin, Y. Si, S. C. Zhang, J. Y. Yu and B. Ding, *Nat. Commun.*, 2021, **12**, 6599.

32 Q. Liu, L. Tang, J. Li, Y. Chen, Z. Xu, J. Li, X. Chen and F. Meng, *J. Mater. Sci. Technol.*, 2022, **130**, 166–175.

33 J.-H. Oh, J. Kim, H. Lee, Y. Kang and I.-K. Oh, *ACS Appl. Mater. Interfaces*, 2018, **10**, 22650–22660.

34 K. Xie, Y. Cao, Z. He, K. Wang, J. Ding, I. MacGillivray, A. Skvortsov, X. Qiu and D. Li, *Appl. Phys. A*, 2022, **128**, 896.

35 L. Yang, J. W. Chua, X. Li, Y. Zhao, B. Q. Thai, X. Yu, Y. Yang and W. Zhai, *Chem. Eng. J.*, 2023, **469**, 143896.

36 S. C. Pinto, A. A. P. M. Paula, V. Romeu, L. Godinho and I. Duarte, *Metals*, 2020, **10**, 768.

37 J.-H. Oh, J.-S. Kim, V. H. Nguyen and I.-K. Oh, *Composites, Part B*, 2020, **186**, 107817.

38 D. Lahiri, S. Das, W. Choi and A. Agarwal, *ACS Nano*, 2012, **6**, 3992–4000.

39 Y. Zhao, J. W. Chua, Y. Zhang and W. Zhai, *Composites, Part B*, 2023, **250**, 110454.

40 J. Liang, F. Ye, Y. Cao, R. Mo, L. Cheng and Q. Song, *Adv. Funct. Mater.*, 2022, **32**, 2200141.

41 Y. J. Zhao, Y. N. Zhang, C. R. Yang and L. F. Cheng, *Carbon*, 2021, **171**, 474–483.

42 W. Huang, W. Gao, S. Zuo, L. Zhang, K. Pei, P. Liu, R. Che and H. Zhang, *J. Mater. Chem. A*, 2022, **10**, 1290–1298.

43 X. Lan, Y. Hou, X. Dong, Z. Yang, B. Q. Thai, Y. Yang and W. Zhai, *ACS Appl. Mater. Interfaces*, 2022, **14**, 15360–15369.

44 X. Ge, G. Tay, Y. Hou, Y. Zhao, P. J. Sugumaran, B. Q. Thai, C. K. Ang, W. Zhai and Y. Yang, *Carbon*, 2023, **210**, 118084.

45 W. Huang, Q. Qiu, X. Yang, S. Zuo, J. Bai, H. Zhang, K. Pei and R. Che, *Nano-Micro Lett.*, 2022, **14**, 96.

46 W. Huang, S. Wang, X. Yang, X. Zhang, Y. Zhang, K. Pei and R. Che, *Carbon*, 2022, **195**, 44–56.

47 J. Xu, X. Zhang, Z. B. Zhao, H. Hu, B. Li, C. L. Zhu, X. T. Zhang and Y. J. Chen, *Small*, 2021, **17**, 2102032.

This journal is © The Royal Society of Chemistry 2023

J. Mater. Chem. A, 2023, **11**, 23452–23462 | **23461**

48 J. Tang, N. Liang, L. Wang, J. Li, G. Tian, D. Zhang, S. Feng and H. Yue, *Carbon*, 2019, **152**, 575–586.

49 X. F. Yu, L. Wang, J. W. Liu, S. Y. Xue, L. T. Yang, X. Li, J. Zhang, L. S. Xing, G. Y. Chen, M. Wang and R. C. Che, *J. Mater. Chem. C*, 2019, **7**, 2943–2953.

50 J. Qiu, J. Liao, G. Wang, R. Du, N. Tsidaeva and W. Wang, *Chem. Eng. J.*, 2022, **443**, 136475.

51 J. Qiao, X. Zhang, C. Liu, L. Lyu, Y. Yang, Z. Wang, L. Wu, W. Liu, F. Wang and J. Liu, *Nano-Micro Lett.*, 2021, **13**, 75.

52 W. H. Gu, J. Q. Sheng, Q. Q. Huang, G. H. Wang, J. B. Chen and G. B. Ji, *Nano-Micro Lett.*, 2021, **13**, 1–16.

53 J. J. Yang, J. Q. Wang, H. Q. Li, Z. Wu, Y. Q. Xing, Y. F. Chen and L. Liu, *Adv. Sci.*, 2022, **9**, 2101988.

54 W. Deng, T. Li, H. Li, R. Niu, A. Dang, Y. Cheng and H. Wu, *Carbon*, 2023, **202**, 103–111.

55 Y. Qian, Y. Luo, A. Y. Haruna, B. Xiao, W. Li, Y. Li, T. Xiong, Q. Jiang and J. Yang, *Small*, 2022, **18**, 2204303.

56 H. Zhao, X. Xu, Y. Wang, D. Fan, D. Liu, K. Lin, P. Xu, X. Han and Y. Du, *Small*, 2020, **16**, 2003407.

57 W. Deng, T. Li, H. Li, A. Dang, X. Liu, J. Zhai and H. Wu, *Carbon*, 2023, **206**, 192–200.

58 F. Wang, Y. Liu, H. Zhao, L. Cui, L. Gai, X. Han and Y. Du, *Chem. Eng. J.*, 2022, **450**, 138160.

59 S. Li, X. Tang, Y. Zhang, Q. Lan, Z. Hu, L. Li, N. Zhang, P. Ma, W. Dong, W. Tjiu, Z. Wang and T. Liu, *ACS Appl. Mater. Interfaces*, 2022, **14**, 8297–8310.

60 M. Šilhavík, P. Kumar, Z. A. Zafar, R. Král, P. Zemenová, A. Falvey, P. Jiříček, J. Houdková and J. Červenka, *ACS Nano*, 2022, **16**, 19403–19411.

61 A. A. Balandin, *Nat. Mater.*, 2011, **10**, 569–581.

62 M. J. Oh, J. H. Lee and P. J. Yoo, *Adv. Funct. Mater.*, 2021, **31**, 2007392.

63 J. Xu, X. Zhang, Z. Zhao, H. Hu, B. Li, C. Zhu, X. Zhang and Y. Chen, *Small*, 2021, **17**, 2102032.

64 Y. Hou, J. Quan, B. Q. Thai, Y. Zhao, X. Lan, X. Yu, W. Zhai, Y. Yang and B. C. Khoo, *J. Mater. Chem. A*, 2022, **10**, 22771–22780.

23462 | *J. Mater. Chem. A*, 2023, **11**, 23452–23462

This journal is © The Royal Society of Chemistry 2023